DE GRUYTER Corros Rev 2023; 41(5): 545–564

Original Article

Mariia Zimina*, Stefan Ritter, Bojan Zajec, Marc Vankeerberghen, Liberato Volpe, Anna Hojná, Rik-Wouter Bosch, Fabio Scenini, Zaiqing Que, Alberto Sáez-Maderuelo, P. Jill Meadows, Michael Grimm, Matthias Herbst, Andraz Legat, Agostino Maurotto, Radek Novotny and Hans-Peter Seifert

Effect of surface machining on the environmentally-assisted cracking of Alloy 182 and 316L stainless steel in light water reactor environments: results of the collaborative project MEACTOS

https://doi.org/10.1515/corrrev-2022-0121
Received December 23, 2022; accepted April 6, 2023;

Abstract: The main objective of the EU-funded project mitigating environmentally-assisted cracking through optimisation of surface condition (MEACTOS) was to gain knowledge on the ability of different surface machining procedures to mitigate environmentally-assisted cracking (EAC) in typical light water reactor structural materials and environments. Surfaces of cold-worked (CW) type 316L austenitic stainless steel and nickel-based weld metal Alloy 182 flat tapered tensile specimens were machined using different processes. EAC initiation susceptibility of these specimens was evaluated using constant extension rate tensile (CERT) tests under simulated boiling water reactor (BWR) and pressurized water reactor (PWR) conditions and assessed using constant load experiments. More than a hundred tests were performed covering about 10 years of autoclave testing time. Only minor or no measurable improvements in EAC initiation susceptibility as a function of surface treatments (grinding or advanced machining) compared to the standard industrial face milling were demonstrated. In most cases, the stress thresholds for EAC initiation determined in constant load tests confirmed the trend obtained from CERT tests. This paper summarises the most important results and conclusions concerning the EAC initiation behaviour for the CW 316L and Alloy 182 under reducing PWR and oxidizing BWR conditions.

Article note: This article is a special contribution associated to a presentation made in the Nuclear Corrosion Symposium at EUROCORR2022, Berlin, Germany, Aug 28 to Sep 1, 2022.

***Corresponding author: Mariia Zimina**, Interface Analysis Centre, H.H. Wills Physics Laboratory, University of Bristol, Tyndall Avenue, Bristol, BS8 1TL, UK; and Centrum vyzkumu Rez (CVR), Rez, Czech Republic, E-mail: m.zimina@bristol.ac.uk. https://orcid.org/0000-0002-1535-347X
Stefan Ritter and Hans-Peter Seifert, Paul Scherrer Institute (PSI), Villigen, Switzerland, E-mail: stefan.ritter@psi.ch (S. Ritter), hans-peter.seifert@psi.ch (H.-P. Seifert). https://orcid.org/0000-0003-4430-4877 (S. Ritter)
Bojan Zajec and Andraz Legat, Slovenian National Building and Civil Engineering Institute (ZAG), Ljubljana, Slovenia, E-mail: bojan.zajec@zag.si (B. Zajec), andraz.legat@zag.si (A. Legat)
Marc Vankeerberghen and Rik-Wouter Bosch, SCK CEN, Mol, Belgium, E-mail: marc.vankeerberghen@sckcen.be (M. Vankeerberghen), rik-wouter.bosch@sckcen.be (R.-W. Bosch)
Liberato Volpe and Fabio Scenini, Materials Performance Centre, University of Manchester, Manchester, UK, E-mail: liberato.volpe@ukaea.uk (L. Volpe), fabio.scenini@manchester.ac.uk (F. Scenini)
Anna Hojná, Centrum vyzkumu Rez (CVR), Rez, Czech Republic, E-mail: anna.hojna@cvrez.cz
Zaiqing Que, VTT Technical Research Centre of Finland, Espoo, Finland, E-mail: zaiqing.que@vtt.fi
Alberto Sáez-Maderuelo, Centro de Investigaciones Energéticas, Medioambientales y Tecnológicas (CIEMAT), Madrid, Spain, E-mail: alberto.saez@ciemat.es
P. Jill Meadows, Jacobs, Warrington, UK, E-mail: jill.meadows@jacobs.com
Michael Grimm and Matthias Herbst, Framatome GmbH, Erlangen, Germany, E-mail: michael.grimm@framatome.com (M. Grimm), matthias.herbst@framatome.com (M. Herbst)
Agostino Maurotto, Nuclear AMRC, Sheffield, UK, E-mail: agostino.interim@gmail.com
Radek Novotny, JRC, Petten, The Netherlands, E-mail: radek.novotny@ec.europa.eu

Keywords: initiation; light water reactor; stainless steel; stress corrosion cracking; weld metal.

1 Introduction

The combination of applied tensile stresses and chemical environment can cause environmentally-assisted cracking (EAC), or its subcategory occurring under constant load – stress corrosion cracking (SCC), in austenitic stainless steels (SSs) and nickel-based alloys. These materials are widely used in the primary circuit of light water reactors (LWRs) due to their high corrosion resistance and good mechanical properties, e.g. ~50–70 % ductility (Griffiths 2019; Kowaka 1976; Maziasz and Busby 2012; Miki et al. 1978; Moss et al. 2018; Takaku and Ushirogochi 1977; Vaillant et al. 2007; Yonezawa 2012). Intergranular SCC in austenitic SS and Ni-alloys (Alloy 600 and 182) in LWR environments are closely related phenomena and show very similar crack growth rates and parameter dependencies, e.g., for the effect of electrochemical potential, harmful anions like chloride and sulphate, stress intensity factor, sensitization or yield stress/hardness/cold-work. The main differences are the specific effect of hydrogen at low electrochemical potential with a SCC peak at the Ni/NiO boundary and the stronger temperature dependency (higher activation energy) in the Ni-alloys as wells as the different GB chemistry and grain structure as well as a higher hot cracking susceptibility. Nickel-based filler metals, such as Alloy 82 and 182 usually used for Alloy 600 weldments, have been used for numerous decades as a weld metal for dissimilar weldments between ferritic and austenitic SS in the primary water of LWR components due to their suitable thermal expansion coefficient (Lee et al. 2007). More resistant weld metals, Alloy 52 and 152, are used in newer plant designs, in e.g. Alloy 690 weldments (Moss et al. 2018), however considerable amount of LWRs still use Alloy 182 as a weld metal. Water SCC of Alloy 182 has been a concern for decades and is the subject of numerous research studies (MRP 2004; Ritter 2020; Scott and Combrade 2019; Vaillant et al. 2007). Under certain load-environment conditions, SCC and primary water SCC cause subcritical failure similar in appearance to brittle behaviour of the otherwise ductile material. The resulting SCC cracks can be sharp and can only be detected in the later stages of EAC, making their detection during the LWR operation complicated. In addition to the environmental factor, tensile stresses can be present in SS components as residual stress from manufacturing introduced from weld solidification, or through different surface finishing processes (Chang et al. 2019), and can impact their long-term operation in LWRs (Du et al. 2019; Ford and Andresen 1994; Scott and Combrade 2019). Non-sensitized type 316L and 304 SSs are used for cooling water piping and reactor core internals in pressurized (PWR) and boiling (BWR) water reactors, such as baffle-to-former bolts. For a long time, type 316L SS had been considered to be non-susceptible to SCC in high-temperature water (Gras 1991). In 2001, the first SCC case was found in the heat-affected zone of core shroud welds at Fukushima-Daiichi 3, BWR plant in Japan. The observed SCC cracks were located in the cold-worked (CW) layer from applied surface machining. Since then, several hundred cases have been observed in more aggressive oxidizing BWR normal water chemistry (NWC) (Horn et al. 1997) as well as in reducing PWR environment (Couvant et al. 2006; Tribouilloy et al. 2007).

The EU-funded project MEACTOS (mitigating environmentally-assisted cracking through optimisation of surface condition) (Ritter 2022a) was proposed and conducted by a consortium of 15 partners from 12 countries (Spain, France, Finland, Czech Republic, Belgium, Germany, Slovakia, Romania, UK, The Netherlands, Slovenia, and Switzerland), comprising research laboratories (VTT, SCK CEN, CVR, CIEMAT, PSI, JRC, RATEN, ZAG), universities (University of Manchester, STUBA), nuclear component suppliers (NAMRC, ENSA), utility (EdF), an engineering company (Jacobs) and plant designer (Framatome GmbH). Several publications were recently produced as a result of this collaboration (Hojná et al. 2020; Hojná et al. 2022; Que et al. 2022a; Que et al. 2021; Que et al. 2022b; Vankeerberghen and Bosch 2022; Vankeerberghen et al. 2022).

In the MEACTOS project, the effect of surface treatments on the EAC initiation susceptibility of a 13 % CW austenitic SS 316L and non-CW nickel-based Alloy 182 weld metal were studied in simulated LWR environments. Four surface finishes were investigated, two advanced machined surfaces (SAM1 and SAM2) were compared to a ground reference surface (RS) and a face milled (STI) one. The surface treatment effect on local subsurface microstructure was studied. The effect of the ultra-fine grained surface layer (UFGL), produced by different machining processes, on the surface oxidation was studied. The susceptibility of the studied materials to EAC initiation was assessed using a series of slow constant extension rate tensile (CERT) and constant load tensile (CLT) tests. CERT testing was used for the materials screening and accelerated assessment of the characteristic critical stress (CC stress) required for EAC initiation. The CC stress values were used to define the loading for the CLT testing phase, reducing the number of tests required. In this paper, the term EAC is used to describe cracking developed during CERT accelerated testing while the cracking which occurred under constant load will be described as SCC.

Although, SCC is a subcategory of EAC, it is important to distinguish between the two testing processes and their character. The accelerated EAC test methodology was adopted and optimized from an earlier collaborative project MICRIN/NUGENIA (Bosch et al. 2021).

Additionally, the effect of shot peening on the EAC initiation of Alloy 182 was studied during the MEACTOS project, but those results are reported elsewhere (Vankeerberghen et al. 2022).

Collected data were further analysed using ANOVA (ANalysis Of VAriance) to evaluate the statistical significance of the particular studied effects, such as environment-surface combination or the environmental effect for PWR and BWR/NWC chemistries.

This paper summarises noticeable findings on the effect of surface treatment on EAC initiation susceptibility of CW 316L SS and Alloy 182 acquired during the MEACTOS project and provides some recommendations for further improvements in laboratory testing methodology and for LWR operators and regulatory bodies.

2 Materials and methods

2.1 Materials and specimens

Type 316L austenitic SS and Alloy 182 were used in this study. CW was applied to the as-received 316L to increase its EAC susceptibility (Couvant et al. 2006). A SS plate was cut into smaller panels, which were cold-rolled in several runs down to ~13 % of thickness reduction. The selected level of CW represents a compromise between increased SCC susceptibility and maintains a level corresponding to plant representative material condition. Alloy 182 was fabricated as a multilayer “overlay” on the Alloy 82 clad carbon low-alloy steel base plate in the stress-relieved (~600 °C for 15 min) condition. Schematics of the materials and main manufacturing directions are provided in Figure 1. Chemical compositions of the CW 316L SS and Alloy 182 are listed in Table 1. Materials tensile properties (yield strength and ultimate tensile strength (UTS)) according to ASTM E8 standard) at 300 °C and $1.6 \times 10^{-4}\ \mathrm{s}^{-1}$ and $5 \times 10^{-8}\ \mathrm{s}^{-1}$ strain rates are summarised in Table 2.

Blocks of the materials were further machined using: (1) STI, (2) SAM1 - advanced machining with supercritical CO_2 cooling without lubrication and (3) SAM2 – advanced machining with supercritical CO_2 cooling with dissolved minimum quantity lubrication oil. The machining was performed using coated carbide indexable inserts of suitable grade in roughing cutting conditions. An overview of the surface machining treatments can be found in Table 3. For Alloy 182, only STI, SAM2 and RS surfaces were studied.

After surface machining, test specimens were manufactured using electric discharge machining (EDM). Flat tapered tensile specimens (Figure 1) were cut in the T-L plane (representing the most SCC susceptible orientation) with the following dimensions: 3 mm thickness, 20 mm gauge length, and 6–8 mm gauge width for CW 316L and 6–10 mm for Alloy 182. One surface of each tapered specimen had either an STI, SAM1 or SAM2 surface, whereas the opposite surface was prepared by wet grinding using up to ISO/FEPA P2000 (1000 grit) SiC paper as reference (RS).

2.2 Experimental procedure

All surface conditions for the two materials were analysed prior to EAC testing using scanning electron microscopy (SEM) and X-ray diffraction (XRD) residual stress measurements. Two test phases have taken place to assess the EAC susceptibility of the studied materials. The first phase consisted of accelerated EAC initiation testing using CERT testing of flat tapered tensile specimens to determine the CC stress for EAC initiation. In the second phase, CLT tests with several acceleration parameters including temperature and environment were performed. These tests and their parameters are further described in following sections.

2.2.1 Microstructural characterization: Material characterization was performed prior to EAC testing on coupon specimens extracted from sections of the CW 316L austenitic SS and of the Alloy 182. Small pieces of materials representing either the T-S or L-S planes, as is shown in Figure 1, were cut by EDM, mounted in bakelite and metallographically polished. The polishing method consisted of mechanical grinding using SiC papers from P240 to P4000 SiC grit, followed by polishing using diamond (3 and 1 µm) solution and final polishing using a 24–40 nm silicon oxide polishing suspension. After the last polishing step, the specimens were carefully rinsed with soapy water, ultrasonically cleaned with deionized water at 25 °C for 15 min, rinsed with ethanol and then dried in a stream of hot air. The microstructure was analysed by SEM using secondary electron (SE) and back-scatter electron (BSE) imaging. Microstructural analyses including electron diffraction and energy dispersive X-ray spectrometry (EDS) were performed using a FEI LaB6 Tecnai T20 analytical scanning/transmission electron microscope (TEM) operated at 200 kV. A field emission gun - focussed ion beam FEI Helios 660 Nanolab FIB-SEM was used to prepare the electron transparent specimen with the in-situ lift out technique and thinned to electron transparency with the Ga + ion beam. A final polishing at 2 kV was performed to minimize the damage from the Ga + beam on the specimen. Topographic surface measurements were obtained using a Keyence VK-X200K 3D laser scanning confocal microscope.

Post-EAC testing characterization was conducted by each partner after CERT and CLT tests using SEM. After CERT testing, the position of the last crack was identified. The last crack was defined as the crack located farthest away from the minimum cross-section which therefore occurred at lowest tensile stress due to the tapered geometry of the specimen. This position was used to determine the EAC critical stress which was used to calculate the CC stress value for each surface treatment – material – environment condition (see Section 2.2.3). After the CLT tests, the locations, surface density, depth and character of EAC cracks were analysed using SEM.

2.2.2 XRD residual stress measurements: Residual stress analysis of the materials was performed by XRD technique using a Proto LXRD unit. Monochromatic radiation from a Mn-Kα tube and an acceleration voltage of 25 kV at 25 mA were used for all measurements. The stress analyses were conducted using the $\sin 2\Psi$ method and a round 1 mm aperture. The residual stress was measured in the transverse and longitudinal directions in respect to the machining feed direction on 11 angles and along a line coincident with the centre of the machining tool where possible. A proto electropolishing unit with electrolyte A

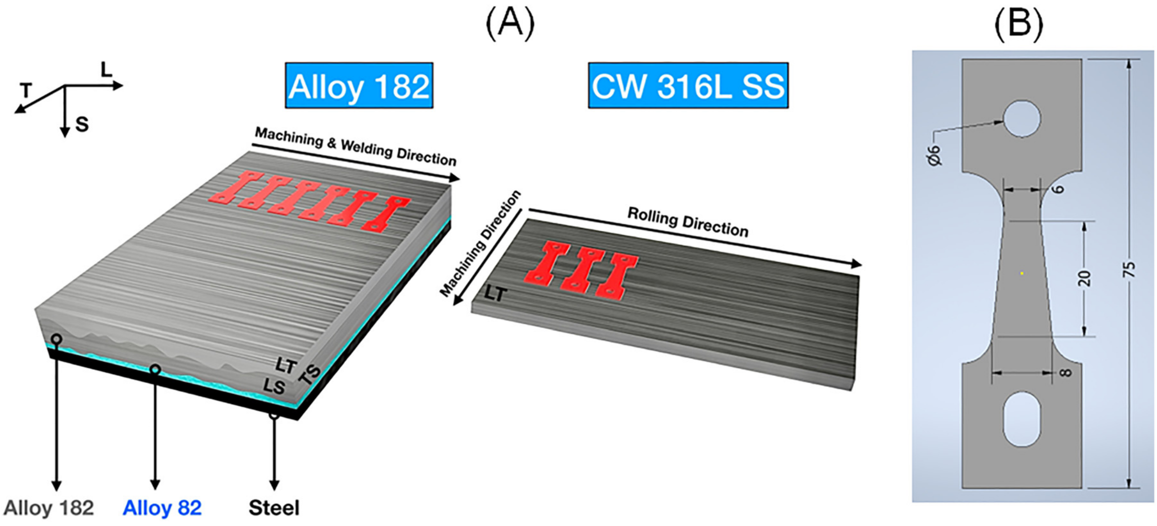

Figure 1: Schematic representation of tapered specimen extraction from the main plate: (A) Diagrams showing the rolling and welding directions, as well as longitudinal (L), transverse (T) and short transverse (S) planes for the as-deposited Alloy 182 weld overlay on the Alloy 82-clad low-alloy steel plate and CW 316L SS; (B) sketch showing principal dimensions flat tapered tensile specimen (in mm).

Table 1: Chemical composition (in wt%) of the 316L austenitic SS and Alloy 182 filler metal.

CW 316L	Fe	Cr	C	Ni	Mn	Nb	Si	Ti
	Bal	17.65	0.017	12.16	1.71	0.005	0.34	0.009
	Mo	Cu	S	Co	P	N	Al	
	2.35	0.059	0.002	0.023	0.018	0.066		
Alloy 182	Fe	Cr	C	Ni	Mn	Nb	Si	Ti
	9.4	14.6	0.032	66.1	6.3	1.97	0.59	0.252
	Mo	Cu	S	Co	P	N	Al	
	0.13	0.043	0.01			n/a	0.019	

Table 2: Mechanical properties of the CW 316L stainless steel and Alloy 182 at 300 °C in air at standard and slow strain rates.

	Yield stress (MPa)		Ultimate tensile strength (MPa)		Elongation to fracture (%)	
	$1.6 \times 10^{-4}\,s^{-1}$	$5 \times 10^{-8}\,s^{-1}$	$1.6 \times 10^{-4}\,s^{-1}$	$5 \times 10^{-8}\,s^{-1}$	$1.6 \times 10^{-4}\,s^{-1}$	$5 \times 10^{-8}\,s^{-1}$
CW 316L	505	570	557	680	8.3	9.0
Alloy 182	358		591		38.8	

Table 3: Surface treatments investigated in the current study.

Surface treatment designation	Type	Description
STI	Standard industrial machining	Face milling with flow coolant
SAM1	Advanced machining	Face milling with supercritical CO_2 cooling, without lubricant
SAM2	Advanced machining	Face milling with supercritical CO_2 cooling, with 1 mL/min minimum quantity lubrication soybean oil
RS	Wet grinding	Grinding with ISO/FEPA SiC paper: P800, P1200, P1500 and P2000

(a NaCl-containing solution) was used to remove the material in order to measure the stresses below the surface.

2.2.3 Accelerated EAC initiation tests: The first test campaign was designed to reach an accelerated screening of the effect of different surface treatments on the EAC initiation susceptibility. Before CERT test, each specimen was exposed to the high-temperature water environment for 7 days to form a stable surface oxide layer (preconditioning) (Robertson 1989; Stellwag 1998). CERT tests of STI/RS tapered specimens with displacement control were performed at nominal strain rates of 5×10^{-8} (only CW 316L SS), 1×10^{-7}, 5×10^{-7} and $1 \times 10^{-6}\,s^{-1}$. For other surface finishes, only the slowest nominal strain rate was used. Due to the chosen design of the tapered specimen, the real strain rate varies along the gauge section and it is higher than the nominal strain rate at the minimum cross-section and lower at the maximum cross-section. With material hardening during the applied load the strain rate is reduced in the minimum cross-section. This at the same time leads to an increase in strain rate in adjoining sections. The CERT tests of CW 316L SS were stopped and the specimen was unloaded when the onset of necking was reached, i.e. when the maximum on the load-extension curve was achieved. For Alloy 182, the CERT tests were continued until specimen failure.

The tests were conducted in two high-temperature water environments: oxidizing BWR/NWC (288 °C, 2 ppm dissolved O_2, high-purity water) and reducing PWR primary water (320 °C, 12 cc/kg dissolved H_2, 1000 ppm B, 2 ppm Li). The dissolved hydrogen value was selected to be at the Ni/NiO transition condition where nickel-based alloys have displayed the highest SCC susceptibility (Attanasio and Morton 2003; Volpe et al. 2021).

After the tests, both surfaces of the CERT tested flat tapered specimens were analysed using SEM at 500*x* magnification. The location of the last EAC crack was identified, and the associated EAC critical stress was calculated based on this location. Criteria for a crack to be considered as an EAC crack were: (1) its surface length was >20 µm and (2) the crack should be predominantly straight and approximately perpendicular to the loading direction during the test. Using this approach, a EAC critical stress was calculated from the maximum load and cross-sectional area at the last crack position for each studied surface. In order to determine the EAC critical stress for each surface treatment from CERT results, the CC stress was introduced using two approaches. For RS/STI specimens which have been tested at three different nominal strain rates, CC stress was estimated by extrapolating the EAC critical stress values to "zero" nominal strain rate. For RS/SAM1 and RS/SAM2 tested only at the lowest nominal strain rate ($1 \times 10^{-7}\ s^{-1}$ for Alloy 182 and $5 \times 10^{-8}\ s^{-1}$ for CW 316L), such extrapolation was not possible, but it was assumed that a plateau was reached with the stresses not decreasing much anymore. CC stress was calculated using an average value of the EAC critical stresses obtained from testing.

2.2.4 ANOVA analysis of CERT data: Various ANOVAs (analyses of variance) (Gelman 2005; Stahle and Wold 1989; Vankeerberghen et al. 2022) were performed to evaluate the statistical significance of some effects. An ANOVA tells us whether there are any statistically significant differences between the dependent variable means for the postulated independent effects. The commonly used α = 5 % criteria to determine statistical significance was applied. If a probability (of the null hypothesis) is lower than 5 %, an effect is statistically significant. If a probability is greater than 5 %, it means that an effect cannot be found statistically (but it does not necessarily mean that it does not exist).

In all analyses the dependent variable was the measured EAC critical stress. The independent variables include laboratory, strain rate, environment and surface finish and their potential interactions.

2.2.5 CLT EAC initiation tests: After the results were evaluated from the first test campaign described in the previous section, CLT testing followed. The same specimen geometry was used for these tests. Before CLT test, each specimen was exposed to the high-temperature water environment for 7 days at zero stress to form stable surface oxide layer (preconditioning), after that the predefined target stress was obtained by constant elongation with nominal strain rate of $1\times10^{-6}\ s^{-1}$. The target stress in the minimum cross section of specimens was set equal to the CC stresses obtained in the CERT test campaign. The applied stress was approximately 12 or 20 % higher than the corresponding yield strength of the CW 316L SS and Alloy 182, respectively. The associated plastic strain calculated from a fit to the tensile curve at 300 °C was approximately 0.5 and 2 % for the CW 316L SS and Alloy 182, respectively. The time to crack initiation in hours was determined by *in-situ* crack length/initiation monitoring using the direct current potential drop technique or by investigation of the surface of the specimen during periodic test interruptions (~ every 250 h for a 1000 *h* test duration). Moreover, the CC stress was evaluated using the same methodology as described in Section 2.2.3.

Testing was performed in two environments: oxidizing BWR and reducing PWR conditions, as described in Section 2.2.3. Different temperatures were tested to study the thermal EAC acceleration effect, and were 288, 340 and 360 °C for BWR and 320, 340 and 360 °C for PWR primary water. In order to preserve the reducing nature of PWR conditions the tests were conducted at a corrosion potential in the nickel-metal stability region but relatively close to the Ni/NiO phase transition, so that the level of dissolved hydrogen was adjusted according to the test temperature from 12 – 20 – 33.4 ccH_2STP/kg (Volpe et al. 2021).

3 Results and discussion

3.1 Microstructural characterization

Figure 2 shows representative surface morphologies for the studied machining processes and reference grinding method for the Alloy 182 and CW 316L.

3.1.1 Alloy 182 weld metal

Figure 2 shows representative surface morphologies for the studied machining processes and reference grinding method. On the STI surface, the machining marks were found to be parallel to the T direction, however their direction changes along the gauge length of the tapered specimens (Figure 2A). Moreover, the STI surface is decorated with some darkly-imaging defects (marked by white arrows), possibly associated with machining processes. The machining marks on SAM2 surface were parallel to each other, and the surface was also decorated with the darkly-imaging spheroidal features (white arrows in Figure 2D). Low voltage qualitative EDS elemental mapping results acquired in T-L plane in Figure 3 show the presence of spheroidal carbon and oxygen-rich features on the STI and SAM2 surfaces. Grinding marks on the RS surface observed to be almost parallel to the loading direction and no major defects were observed on the surface (Figure 2F).

Figure 4 shows BSE cross-sectional views of the near-surface regions subjected to the STI, SAM2 and RS treatments along the T-S plane. The STI Alloy 182 cross-section exhibits a variable UFGL in Figure 4A. A deformed region of about ≥20 µm was observed beneath the UFGL. The presence of fine cracks is observed on the surface (Figure 4A, marked by a white arrow) and associated with the machining-induced local deformation that could further lead to preferential development of SCC or mechanical cracks. Bright field (BF) TEM images of the near-surface region of the STI Alloy 182 (in T-S plane) revealed a well-developed UFGL that varied in depth from ~2 to ~6 µm, as

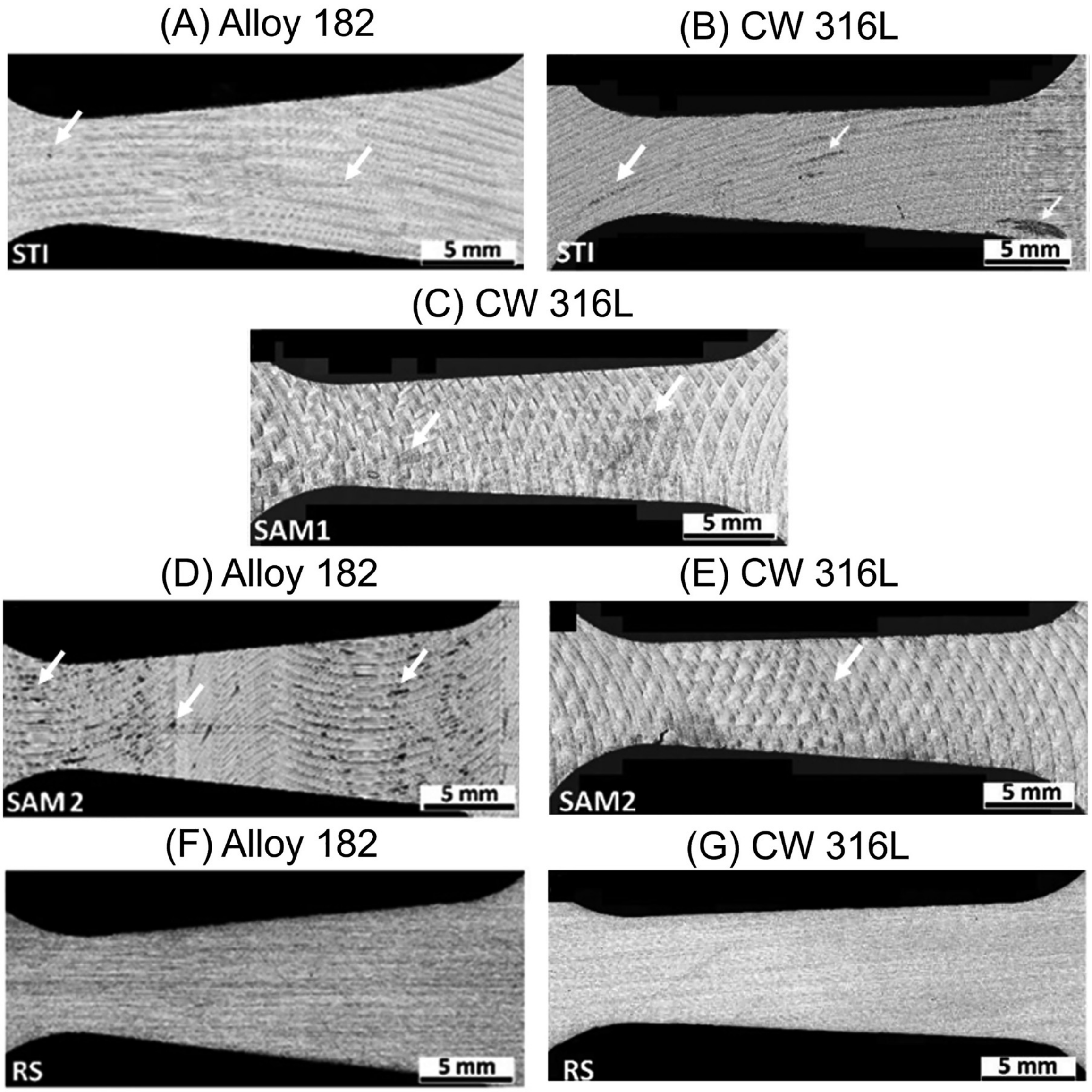

Figure 2: Laser confocal microscopy images showing the morphologies associated with the (A, B) STI, (C) SAM1 (D), (E) SAM2 and (F), (G) RS surface conditions for Alloy 182 and CW 316L, respectively. Arrows show surface C/O contamination analysed by EDS in Figures 3 and 6.

shown in the BF TEM image of Figure 5A. These deformed ultrafine grains ranged from ~15 to 200 nm in size. The SADP in Figure 5B confirmed the randomly-oriented polycrystalline structure, as evidenced from the discrete rings. Additional TEM analysis revealed the highly deformed nature of these grains. Furthermore, a uniform darkly-imaging layer, approximately 20 nm in thickness, was observed on the as-machined surface (Figure 5A); this layer may be associated with C/O contamination of the lubricant oils used during the machining processes.

The SAM2 process induced a more complex near-surface microstructure, as shown in the BSE micrographs in Figure 4B. An UFGL of about 2–3 μm deep is followed by a complex deformed structure and then by the deformed zone with characteristic deformation bands that extend approximately ≥20–30 μm into the specimen. Results of TEM analyses of the SAM2 surface are shown in Figures 5C and D. The BF TEM image shows a portion of the UFGL induced by SAM2 machining process on the T-S plane; these ultrafine grains were predominantly equiaxed and ranged in size from ~15 to ~150 nm. In addition, this TEM image contains a fine lap induced by the SAM2 process. Such defects could act as preferential sites for SCC and mechanical crack initiation. The corresponding SADP in Figure 5C confirmed

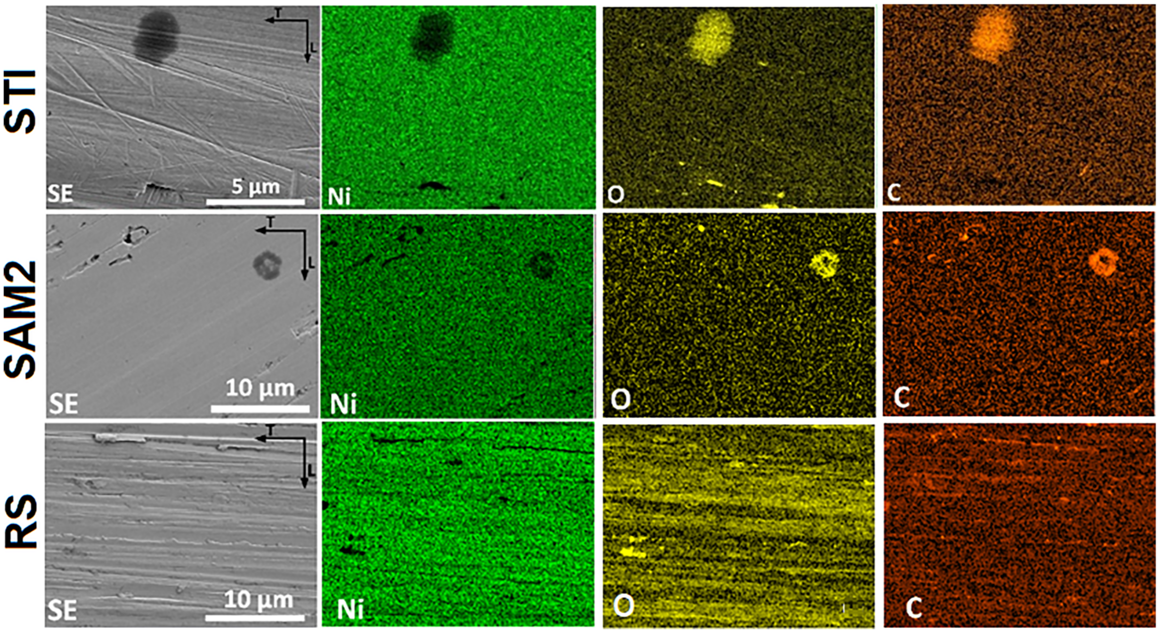

Figure 3: SE image and corresponding EDS maps of the STI, SAM2 and RS surfaces of Alloy 182 in T-L plane showing the nickel and surface contamination with C and O.

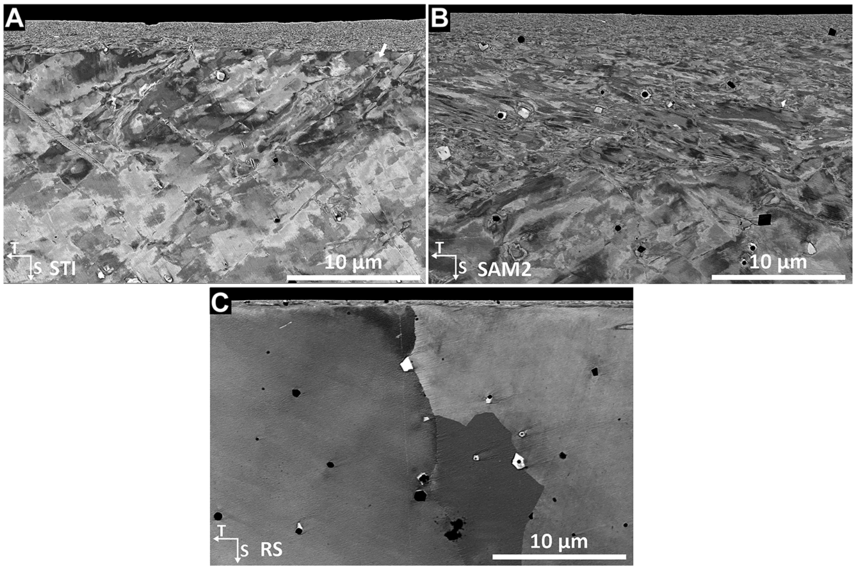

Figure 4: BSE images obtained along the T-S plane of cross-sectional Alloy 182 specimens showing the near-surface machining-induced UFGL generated from (A) STI, (B) SAM2 and (C) RS processes.

the polycrystalline nature of that UFGL. A continuous darkly-imaging surface layer (~15–20 nm in thickness in Figure 5C), possibly associated with the C/O contamination, was observed on the SAM2 machined surface, as previously noted also for the STI condition (see Figure 5A).

The RS surface shows an approx. 300 nm thick UFGL and deformed layers, not visible in the BSE image in Figure 4C. Figure 5E shows a BF TEM image of a representative portion of the UFGL induced by the manual grinding process on the T-S plane. The surface was deformed with several nano-sized grains within the first ~200 nm from the surface. These deformed grains ranged from ~15 nm to ~100 nm in size. The discrete rings shown in the SADP acquired within the UFGL confirmed the presence of a randomly oriented polycrystalline layer (Figure 5F).

A more comprehensive baseline material characterization can be found in (Que et al. 2021; Volpe et al. 2022; Volpe et al. 2020).

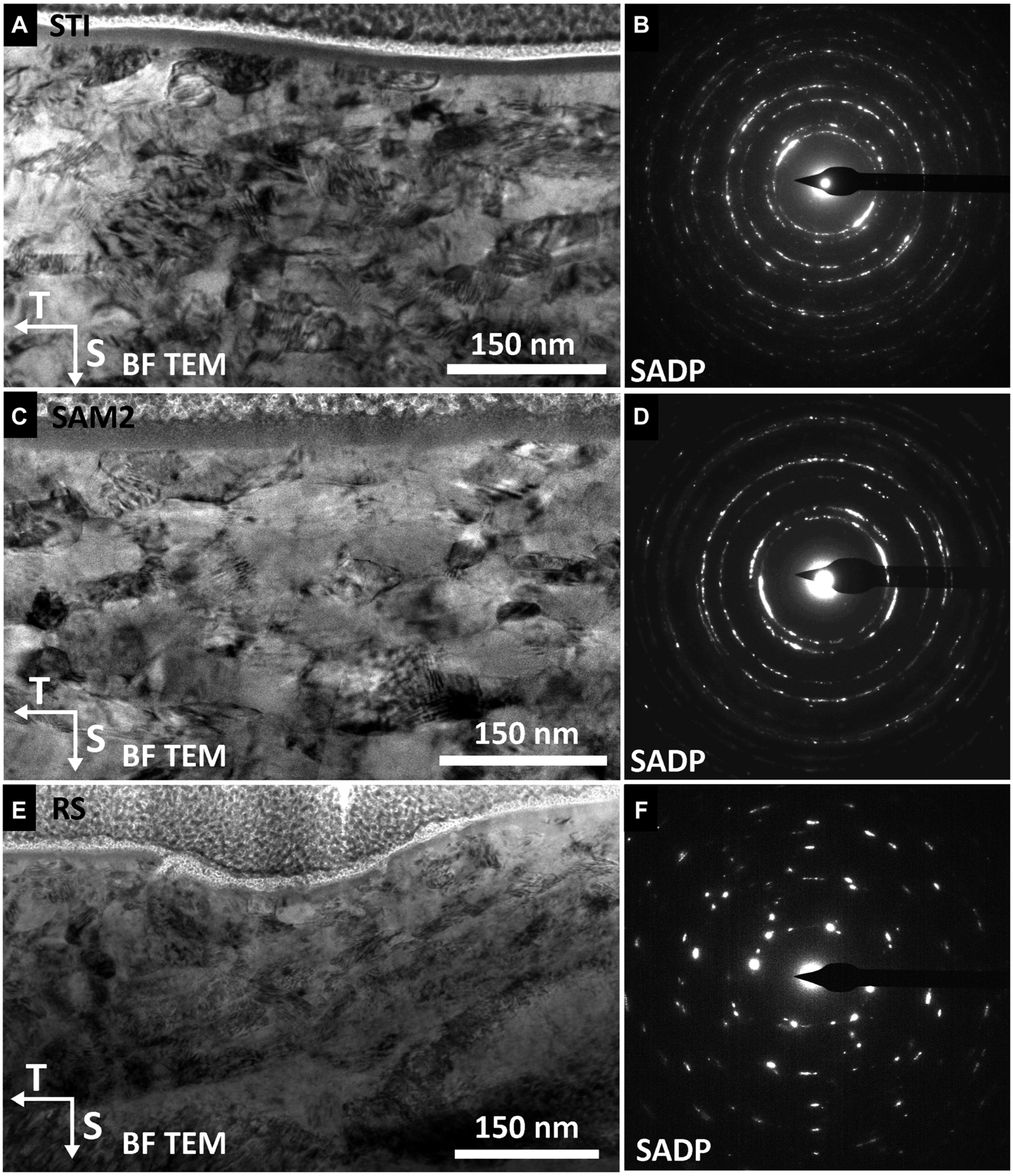

Figure 5: BF TEM image of the UFGL associated with the machined surface on the T-S plane of Alloy 182 and SADP acquired within the UFGL for (A, B) STI, (C), (D) SAM2 and (E), (F) RS surfaces; a continuous darkly-imaging contaminant layer (~15–20 nm in thickness) is observed in (A) and (C).

3.1.2 CW 316L stainless steel

Representative laser confocal microscopy images of the STI, SAM1 and SAM2 and RS surfaces along the T-L plane for the CW 316L SS specimens are shown in Figure 2B, C, E and G. The STI, SAM1, SAM2 surfaces contain numerous darkly-imaging deposits (marked by white arrows in Figure 2B, C and E). Similar features were also present along grinding marks in RS specimens (Figure 2G). The machining marks in advanced machined specimens changed significantly along the gauge length compared to the STI. The EDS analysis showed that the deposits are associated with C/O (Figure 6).

The micrographs in Figure 7 show the effect of the different surface grinding and machining on the near-surface microstructure for the CW 316L SS. BSE images with

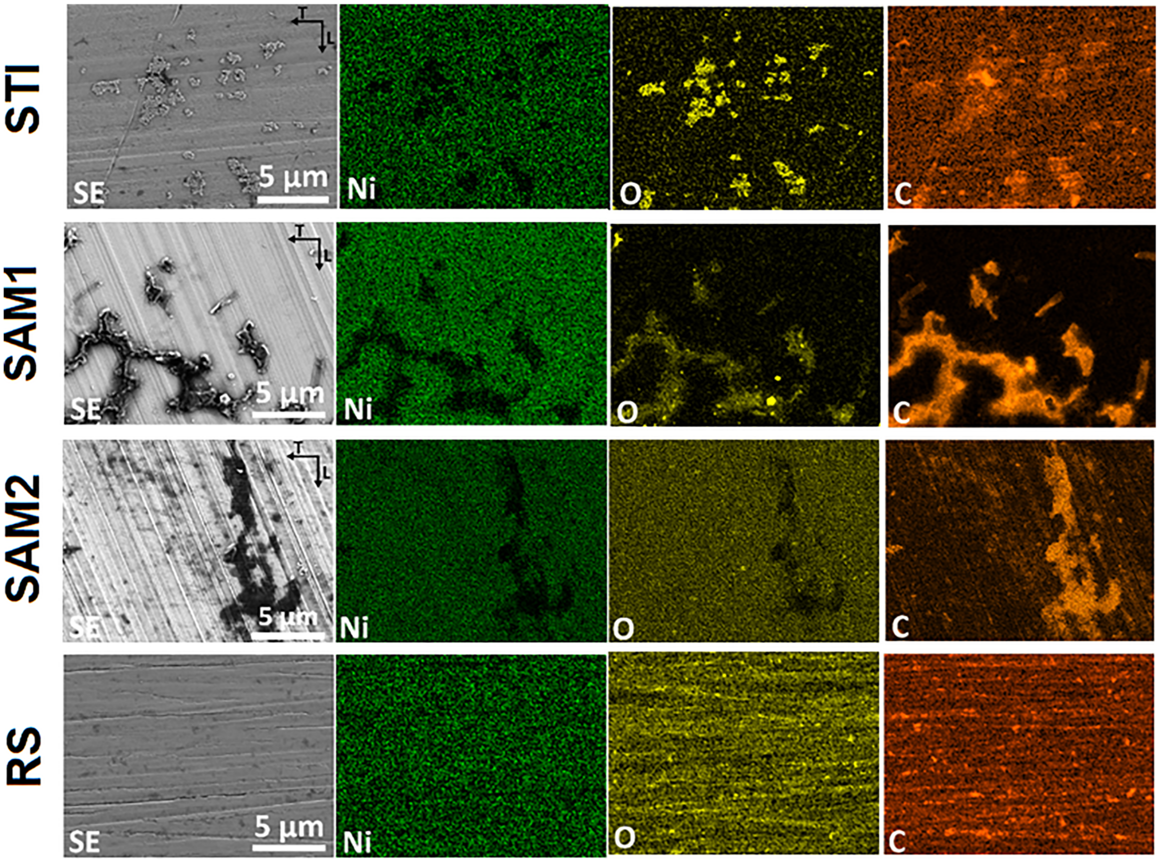

Figure 6: EDS mapping of RS surface in T-L plane of CW 316L SS showing main alloying elements and surface contamination by C and O.

different magnifications of the near-surface regions of T-S cross-sections of all studied surfaces are presented.

The near-surface microstructure associated with the STI machining process was heavily deformed due to the cold-rolling of the 316L plate and the BSE micrographs show also a pronounced bending of slip bands beneath the UFGL (Figure 7A). Such distortion of the slip bands was not observed in the ~13 % cold-rolled 316L microstructure prior to machining. Thus, these features provided guidance in estimating the depth of the machining-induced deformation, which was approximately 30 – 40 µm. The UFGL thickness associated with the STI process was less than 3 µm in depth and varied along the surface (Figure 7B).

Micrographs of the SAM1 surface of the SS specimen are shown in Figure 7C and D. The heavily deformed microstructure along the T-S plane was consisting of UFGL and the CW deformed layer which are not very well defined. In this case, the correct depth of the UFGL was calculated using L-S plane observations, where it was well pronounced (~3 µm). The estimated depth of machining-induced deformation was between ~30 and 40 µm.

Microstructure of SAM2 machined specimens, shown in Figure 7E and F, exhibited a similar morphology to that observed for the CW 316L SAM1 SS (see Figure 7C and D). Heavily deformed microstructure associated with the SAM2 machining and the CW processes was observed. The UFGL thickness was in a range from ~1 to 3 µm (Figure 7F). The deformation induced by machining is represented by bands beneath the UFGL. In this case, the depth of the deformation induced by the SAM2 process was extended up to ~40 µm. In addition, a lap induced by the machining process was observed in the material after SAM2 process; such a defect could possibly affect preferential initiation for SCC and mechanical cracks.

The RS specimen was characterized by a thin UFGL that varied in thickness but was approximately ~500 nm deep (Figure 7G and H). The depth of deformation associated with the RS preparation was estimated to be ~1 µm.

The results of the measurements of UFGL thickness, UFG average grain size and machining-induced deformed layer average thickness for all material-surface conditions are summarised in Table 4.

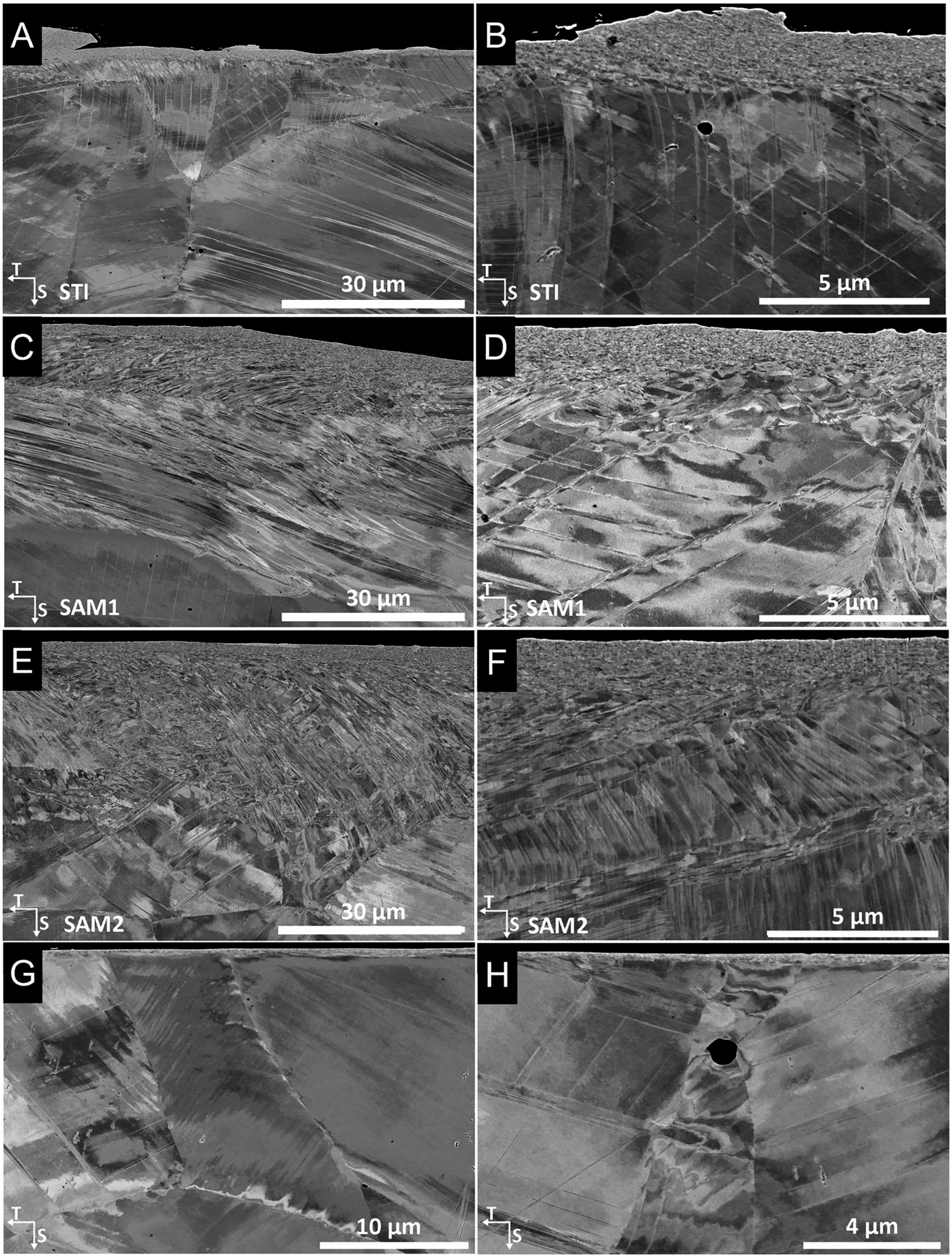

Figure 7: BSE images obtained from cross-sectional specimens showing the near-surface machining-induced UFG and deformed layers generated from the STI, SAM1, SAM2 and RS processes, as well as the deformed region associated with the CW along the T-S plane for the CW 316L SS.

Table 4: Summary of UFGL thickness, grain size and machining-induced deformed layer thickness for the CW 316L and Alloy 182 (Volpe et al. 2020).

Surface treatment	UFGL thickness (µm)/grain size (nm)		Machining-induced deformed layer thickness (µm)	
	CW 316L	Alloy 182	CW 316L	Alloy 182
STI	~1–3 µm/~20–50 nm–300 nm	2–6 µm/~15–200 nm	~30–40	~20+
SAM1	~3 µm/~30–300 nm		~30–40	
SAM2	1–3 µm/~20–300 nm	2–3 µm/~15–150 nm	~30–40	~20–30+
RS	≤~0.5 µm/~15–100 nm	≤~0.5 µm/~15–100 nm	≤~1	≤~2

3.2 XRD residual stress measurements

The residual stress induced by machining was measured using XRD in the longitudinal and transversal directions. Table 5 summarises the results. It was shown that STI, SAM1/SAM2 treatments introduce tensile residual stress in both SS and nickel-based weld metal. Grinding, on the other hand, leads to compressive stresses at the surface of the plates. The large measurement uncertainty in case of Alloy 182 could be caused by the insufficient surface quality of used specimens as well as the effect of strong crystallographic texture due to machining.

3.3 Accelerated EAC initiation tests

The results of the CERT testing for CW 316L SS and Alloy 182 are summarised in the box plots in Figures 8 and 9, respectively. The EAC critical stress and CC stress data are represented as a function of surface treatments using simplified box plots where, besides all EAC critical stress datapoints in the given category, their distribution is presented with 1st and 3rd quartiles and median value (horizontal line in the box). The average EAC critical stress value (which defines the CC stress for the given surface category) is presented by red dash symbol. RS/STI specimens were tested at three different strain rates and their measured EAC critical stress dependency to strain rate was fitted with an exponential function with 90 % confidence interval, and is shown in Figure 10. Its extrapolation to zero strain rate gives CC stress which is also presented as an error bar in the corresponding box plots in Figures 8 and 9. When looking at Figures 8 and 9 the reader has to bear in mind that a flat tapered specimen has two sides, mostly surface-finished differently. One side is RS-finished, the other STI-, SAM1- or SAM2-finished. Hence, CC stress results for STI, SAM1 or SAM2 are reported for specimens that always have an RS finish on the other side. On the contrary, CC stress results for RS are reported for specimens that might have an STI, SAM1 or SAM2 finish on the other side. Then, if RS reporting is not taking into account the other side, it is reported as RS/ALL. If RS reporting is grouped by the other side's finish, it is reported as RS/STI, RS/SAM1 or RS/SAM2.

Table 5: XRD residual stress measurement results for the CW 316L SS and Alloy 182 with different surface treatments in longitudinal and transverse directions.

Surface treatment	Longitudinal (MPa)		Transverse (MPa)	
	CW 316L	Alloy 182	CW 316L	Alloy 182
STI	527 ± 92	63 ± 35	525 ± 99	134 ± 120
SAM1	700 ± 133	–	672 ± 98	–
SAM2	624 ± 187	705 ± 208	623 ± 185	864 ± 332
RS	−270 ± 32	−538 ± 164	−219 ± 6	−352 ± 12

The effects of different surface treatments in reducing PWR and oxidizing BWR/NWC environments on the EAC critical and CC stress values are plotted in Figure 8 for CW 316L SS. This effect was insignificant for this material in both environments. The CC stress was lower for all surface treatments in reducing environment compared to the oxidizing one. Thus, the material appears to be more susceptible to EAC initiation in PWR primary water environment than in BWR/NWC in the loading region close to the corresponding UTS at 300 °C. The UTS for SS at this temperature (557 MPa, see Table 2) was lower than the calculated CC stresses after CERT testing, which can be explained by the dynamic strain ageing (DSA) effect. DSA is associated with the anomalous appearance of serrations in the tensile stress–strain curves at particular test temperatures (for austenitic SS from 300 to 650 °C (Karlsen et al. 2009)) due to the impedance of dislocation glide by their interaction with diffusing solute atom (Mulford and Kocks 1979; Sleeswyk 1958). A strong effect of strain rate on the incidence of DSA was previously reported by (Karlsen et al. 2009; Peng et al. 2004).

It needs to be emphasized that the 13 % CW 316L SS showed a low susceptibility to EAC in the tested environments and little or no "typical" stress corrosion cracks were observed. Thus, the observed difference in CC stress in Figure 8 is more likely related to the temperature effect (320 versus 288 °C) than to the different water chemistry.

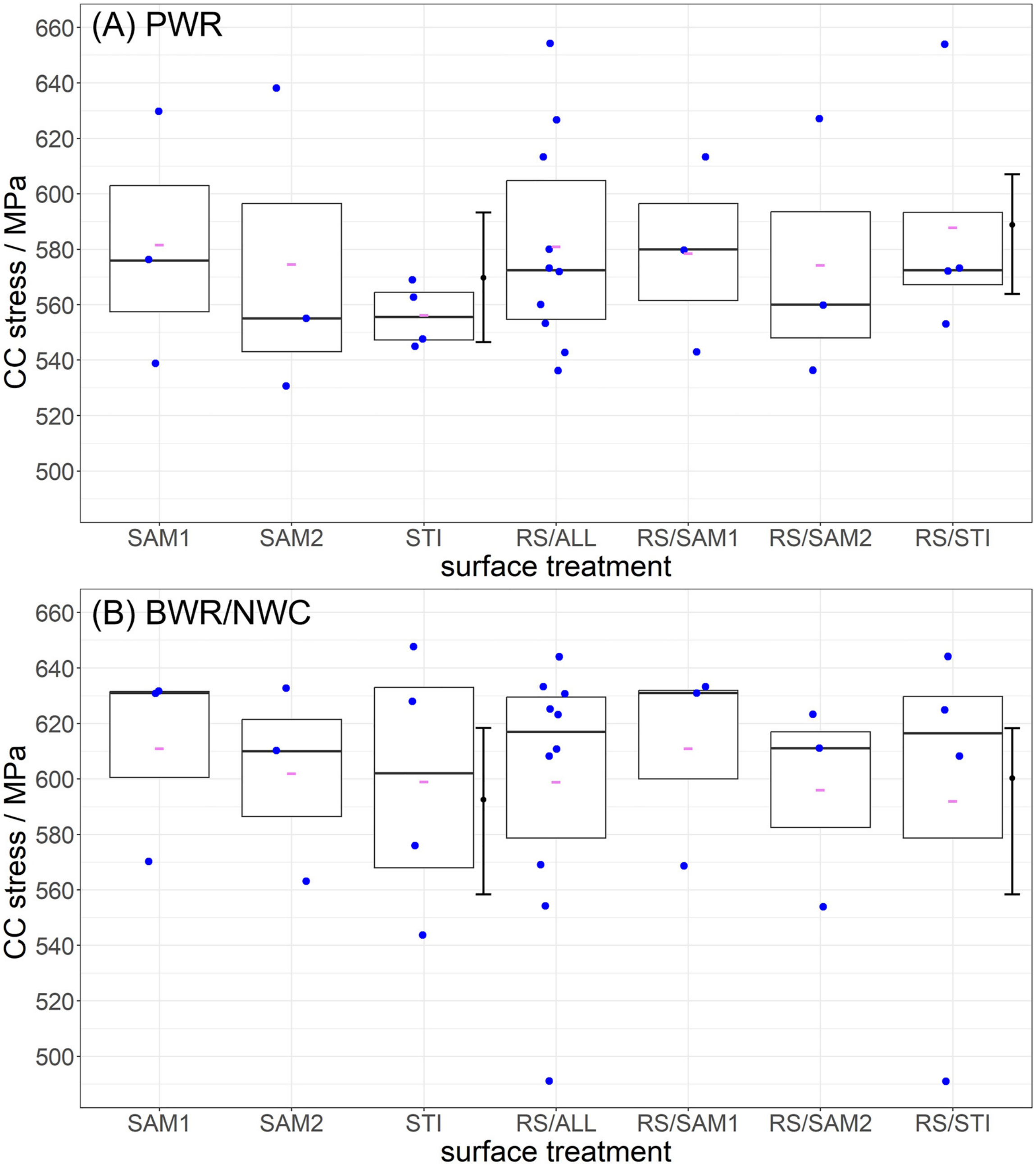

Figure 8: Summary of the measured EAC critical and calculated CC stress data dependence on surface treatments for CW 316L SS in (A) PWR and (B) BWR/NWC environments. The average EAC critical stress value within each category is marked by a red dash, two error bars indicate CC stress obtained by extrapolation to zero strain rate. Other details are described in Section 3.3.

Plots representing the effect of the surface treatment on EAC critical stress and calculated CC stress values for Alloy 182 in PWR and BWR/NWC environments are shown in Figure 9. As expected, generally the Alloy 182 showed a lower resistance to EAC than the CW 316LSS. The results also show that Alloy 182 is more susceptible to EAC under reducing PWR primary water conditions compared to oxidizing BWR/NWC. In PWR, the SAM2 surface performed slightly better compared to the STI and RS surfaces. This effect was not as pronounced in the oxidizing environment. All material-environment combinations showed that the surface machining applied to one side of specimen does not impact the opposite RS side. This is evident from similar values of CC stress in RS/SAMx and RS/STI categories.

Figure 10 shows the strain rate effect on EAC critical stress for STI surface treatment of CW 316L and Alloy 182

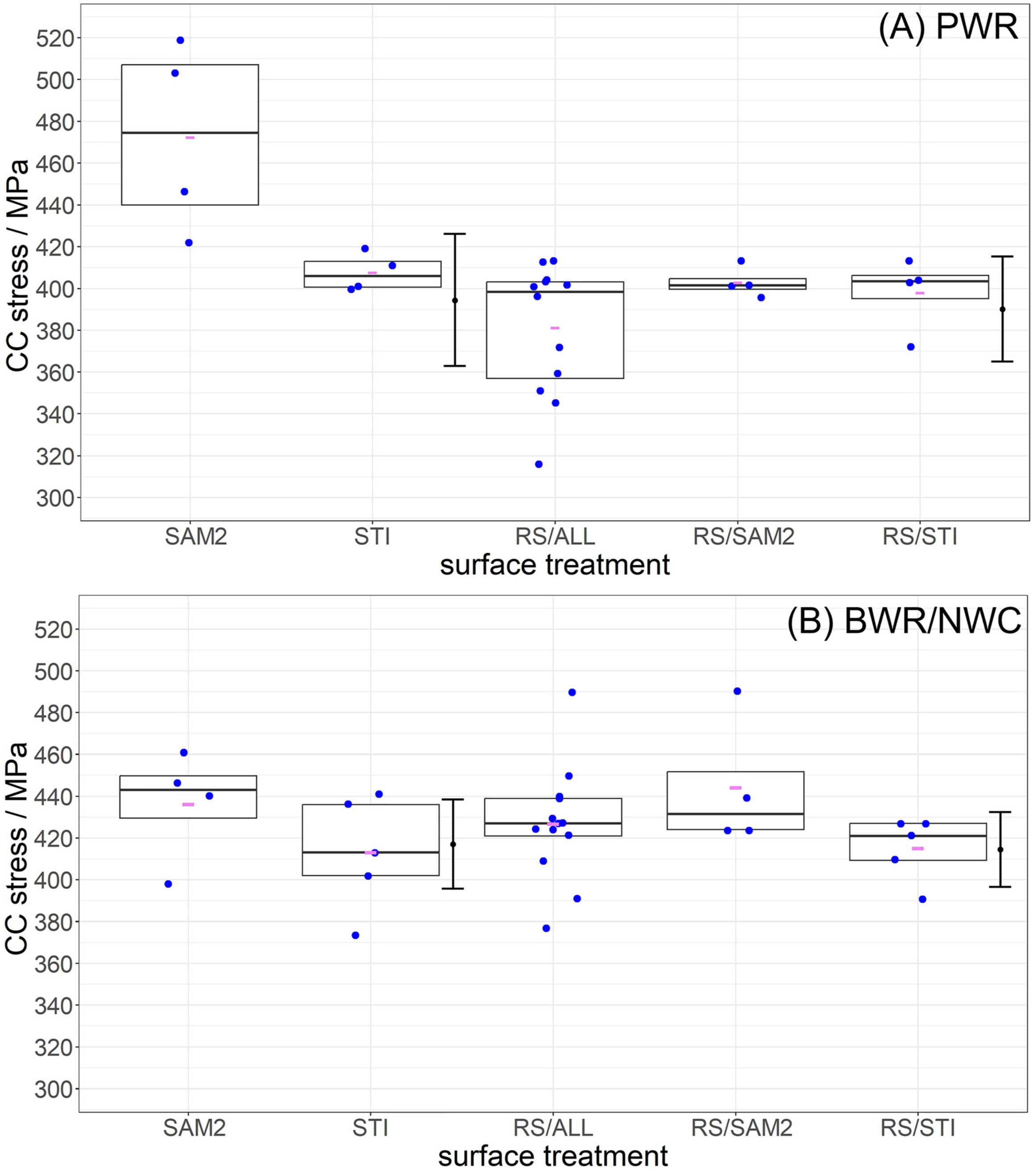

Figure 9: Summary of the measured EAC critical stress and calculated CC stress data dependence on surface treatments for Alloy 182 in (A) PWR and (B) BWR/NWC environments. The average value within each category is marked by a red dash, two error bars indicate CC stress obtained by extrapolation to zero strain rate. Other details are described in Section 3.3.

in PWR and BWR/NWC environments. The calculated CC values are shown using black error bar on the left side of each plot. Similar plots were obtained also for RS surface of RS/STI specimens but are not presented in this paper. Low susceptibility of CW 316L to EAC results in weak or absent strain rate dependence (Figure 10B).

3.4 ANOVA results

3.4.1 Alloy 182 weld metal

The results of CERT testing of Alloy 182 were used for ANOVA analysis. The first analysis considered the four environment-

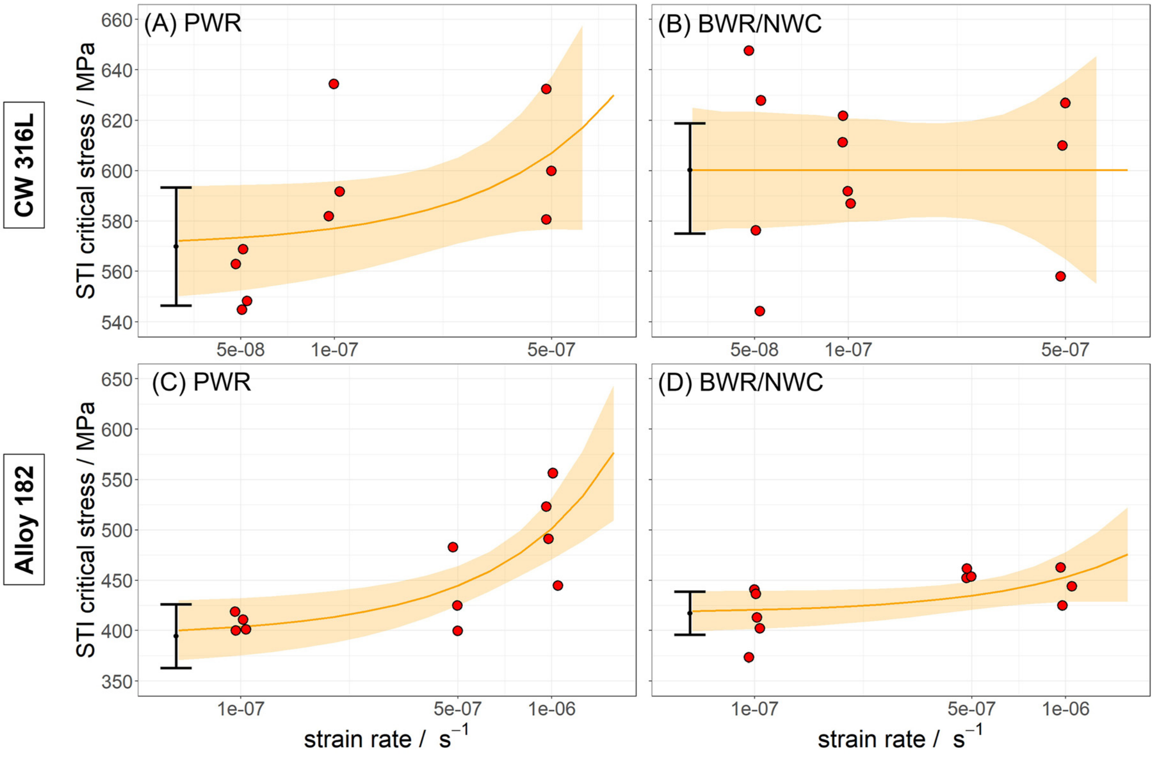

Figure 10: Best exponential fit with 90 % confidence interval to the EAC critical stress values of CW 316L SS and Alloy 182 STI specimens obtained at different strain rates. The obtained CC stress (at zero strain rate) is presented with a black error bar on the left side.

surface finish combinations (PWR or BWR/NWC, RS or STI) separately. The postulated effects were nominal strain rate and laboratory. For all environment-surface finish combinations no effect of the laboratory was observed (listed probability of null hypothesis >5 %) and an effect of the nominal strain rate on the EAC critical stress (listed probability of null hypothesis <5 %) was shown as reported in Table 6. This entails that the CERT test with tapered specimens (being an accelerated type of EAC initiation test) is robust enough for a test matrix spanning over various laboratories; which generally would make it suitable for standardization.

The second analysis considered the two environments (PWR or BWR/NWC) separately. The postulated effects were strain rate and surface finish, whilst laboratory effect was not considered because it was shown above to be insignificant. Both environments showed an effect of strain rate and surface finish (listed probability of null hypothesis <5 %).

The third analysis considered all Alloy 182 CERT data simultaneously. The postulated effects were strain rate, environment, surface finish and the environment – surface finish interaction. Strain rate and environment showed up as an effect (listed probability of null hypothesis <5 %). Surface finish did not show up as a main effect (listed probability of null hypothesis >5 %), but only as an effect in combination with the environment (listed probability of null hypothesis <5 %). This indicates that the effect of surface finish depends on the environment or, vice versa that the effect of the environment depends on the surface finish. The result corresponds to that shown in Figure 9, where the average EAC critical stress value (which defines the CC stress for the given category) for STI is higher than for RS/All in PWR environment, whereas it is lower than for RS/All in BWR/NWC.

3.4.2 CW 316L stainless steel

The results of the ANOVA analysis for the CW 316L SS CERT testing are also summarised in Table 6. The first analysis considered the four environment-surface finish combinations (PWR or BWR/NWC, RS or STI) separately. The postulated effects were nominal strain rate and laboratory. All but one environment-surface finish combination (BWR/NWC-RS) showed no discernible effect of the laboratory on the EAC critical stress (listed probability of null hypothesis >5 %). One dataset had to be excluded from the analyses due to its inconsistency. No discernible effect of laboratory on EAC critical stress was observed. All environment-surface finish

Table 6: ANOVA analyses of Alloy 182 and CW 316L SS – effects on EAC critical stress.

		Alloy 182		
	PWR-RS #21	**PWR-STI #13**	**BWR/NWC-RS #18**	**BWR/NWC-STI #10**
Strain rate	0.83 %	4.13 %	1.79 %	4.28 %
Laboratory	65.38 %	50.99 %	11.17 %	21.29 %
			PWR	**BWR/NWC**
Strain rate			0.00 %	0.07 %
Surface finish			0.64 %	4.32 %
			All	
Strain rate			0.00 %	
Environment			0.12 %	
Surface finish			20.79 %	
Environment × surface finish			0.06 %	
		CW 316L		
	PWR-RS #17	**PWR-STI #10**	**BWR/NWC-RS #19**	**BWR/NWC-STI #11**
Strain rate	86.6 %	9.25 %	79.47 %	70.7 %
Laboratory	74.5 %	45.62 %	2.06 %	19.6 %
	PWR		**BWR/NWC**	
Strain rate	46.8 %		27.89 %	
Laboratory	77.7 %		0.44 %	
Surface finish	85.7 %		24.70 %	
	All			
Strain rate	64.9 %			
Environment	16.5 %			
Surface finish	60.3 %			
Laboratory	60.6 %			

Probability of null hypothesis: <5 % there is a statistically significant effect; >5 % no effect is found.

combination showed no discernible effect of the nominal strain rate on EAC critical stress (listed probability of null hypothesis >5 %). The analysis did not reveal a strain rate effect for CERT test on flat tapered specimens. This might be due to the low susceptibility of the 13 % CW 316L SS to EAC.

The second analysis considered the two environments (PWR or BWR/NWC) separately. The postulated effects were strain rate, surface finish and laboratory. The laboratory effect study demonstrated that the PWR environment showed no discernible effect (listed probability of null hypothesis >5 %) and the BWR environment showed an effect (listed probability of null hypothesis <5 %) on the EAC critical stress. There was no discernible effect of strain rate and surface finish on the EAC critical stress (listed probability of null hypothesis >5 %).

The third analysis considered all CW 316L CERT data simultaneously. The postulated effects were strain rate, environment, surface finish and laboratory. None of the effects were discernible (listed probability of null hypothesis >5 %).

3.5 CLT EAC initiation tests

The results of CLT testing for all surface treatments of CW 316L SS and Alloy 182 for different temperatures and environments (oxidizing BWR/NWC and reducing PWR) are summarised in initiation time versus temperature and EAC critical stress versus initiation time plots in Figures 11 and 13. These graphs also include the datapoints with no observed SCC initiation during the testing time. They are marked by red arrows in the figures. The initiation time for specimens without SCC is represented as the testing time (the real initiation time will be > testing time) and EAC critical stress is the CLT applied stress.

Figure 11 shows initiation time dependence on temperature for the CW 316L SS and Alloy 182 for all studied surface treatments and environments. RS surface datapoints are shown in separate Figure 11B and D for better comparison. The results show that there was no clear effect of the surface treatment for CW 316L SS on the initiation time in all studied environments. The time to initiation is 1000 h for PWR reducing environment for 320–350 °C for majority of tested tapered specimens except one RS/STI specimen. In BWR/NWC, the SCC initiation was observed after 555 h in one SAM2 specimen and was above 1000 h for other surfaces. Initiation time in oxidising BWR/NWC appears to be similar or higher than in reducing PWR for existing datasets. A possible reason for the better EAC initiation behaviour in BWR over PWR environment and a better EAC crack growth behaviour for PWR over BWR might be that initiation is a surface effect, while during the crack growth one has to consider the 3D nature of the crack (Andresen 2008). The potential gradient from crack mouth to crack tip is a driving force for anionic species transport and is only available in oxidizing BWR environment, resulting in a higher crack growth rate in BWR compared to PWR environment. For initiation, the stability (and repair-after-rupture) of the oxide at the surface is more relevant and is determined by the electrode potential. The latter is higher in BWR than in PWR, resulting in better oxide-forming conditions under BWR conditions and, hence, a longer time for initiation.

The SCC cracks observed on each surface were further analysed and their density was calculated after an initial 1000 h and for longer testing times if the cracks were not present after the initial period. It was shown that in oxidizing BWR/NWC environment, the density of cracks on

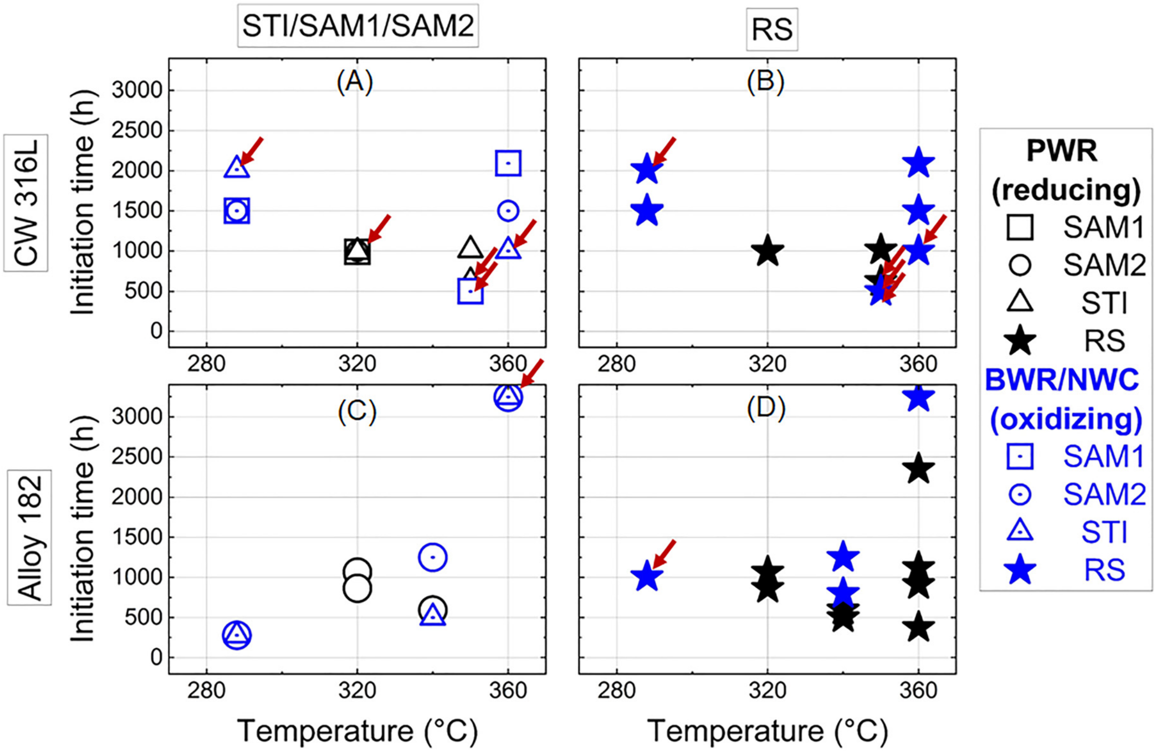

Figure 11: Time to initiation versus temperature plots for all studied surface treatments and environments for the (A and B) CW 316L SS and (C and D) Alloy 182. PWR, black symbols; BWR/NWC, blue symbols.

SAM1 surface was the highest. Machined SAM2 surface was the second highest populated, following by STI surface. The RS surface was the least populated with initiated SCC cracks in BWR/NWC. Crack population in reducing PWR was similar on the STI, SAM1 and RS surfaces. The SAM2 surface was not susceptible to SCC under the studied conditions and no cracks were observed.

The SCC initiation behaviour of Alloy 182 with applied surface treatments differs significantly from that of the CW austenitic SS. Figure 11C and D shows the initiation time on the temperature dependence for the nickel-based alloy with different surface treatments. In Figure 11C, clearly visible decreasing trends of initiation time with temperature are shown only for SAM2 surface with UFGL in PWR environment. Time to initiation in BWR condition, also plot in the graph, is increasing. However, for RS surface, where neither UFGL nor deformed layer was present, no clear dependence was observed. The time to initiation was also found to be overall higher in the oxidizing BWR/NWC environment than in reducing PWR conditions.

The examples of the SCC cracks found in CW 316L and Alloy 182 after CLT testing in PWR and BWR/NWC environments are shown in Figure 12.

In order to compare the EAC critical stress for crack initiation for different surface treatments, the EAC critical stress dependence on initiation time is reported in Figure 13. The results show that the EAC critical stress for both materials is not dependent on the surface treatment or environment.

4 Practical recommendations

The MEACTOS project provided valuable information for the nuclear power plants stakeholders, such as operators, suppliers and nuclear authorities. The results on the influence of the surface treatment effect on EAC susceptibility of CW 316L SS and Alloy 182 used for weldments demonstrated that advanced surface machining methods (SAM) showed a comparable EAC initiation behaviour as standard machining method (STI), i.e. they are not inferior. In combination with benefits like higher cutting speed and less pollution by lubricants, they are a promising alternative and can be used for future applications or if standard methods cannot be used.

The number of key recommendations was suggested in a harmonisation roadmap. An important recommendation is

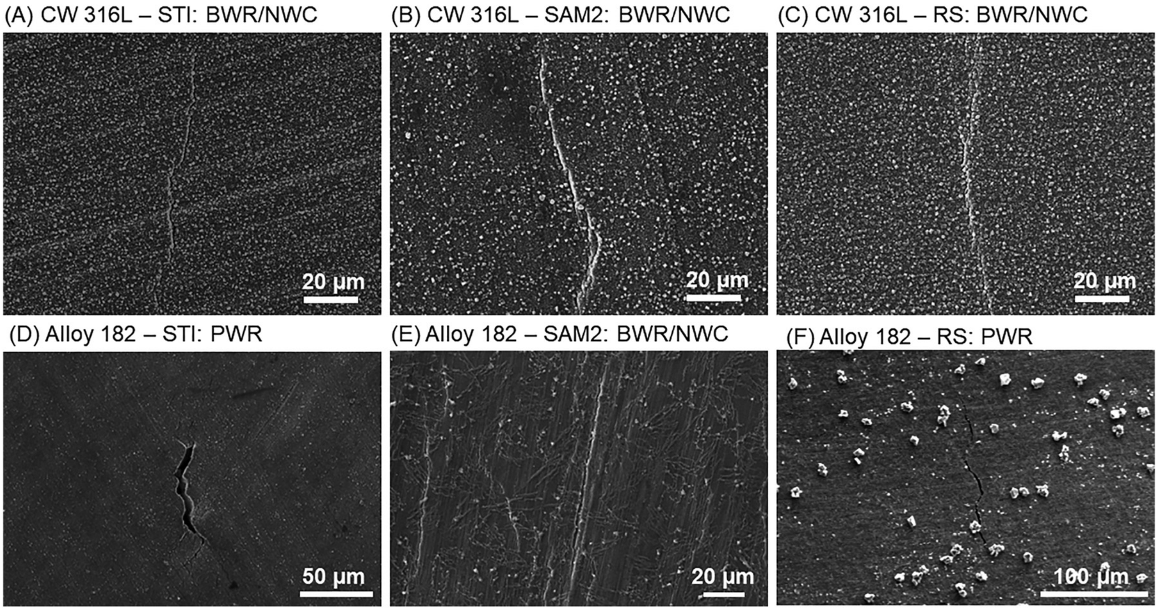

Figure 12: SCC crack appearance in CW 316L SS and Alloy 182 during CLT testing [BWR/NWC 288 °C and PWR 340 °C (STI) and 360 °C (RS)].

that specifications for surface treatments of components in nuclear power plants should be considered by regulators and authorities in their national rules and standards (e.g. hardness and roughness thresholds for different surface treatments). The implementation of a common European guideline based on national rules and existing knowledge

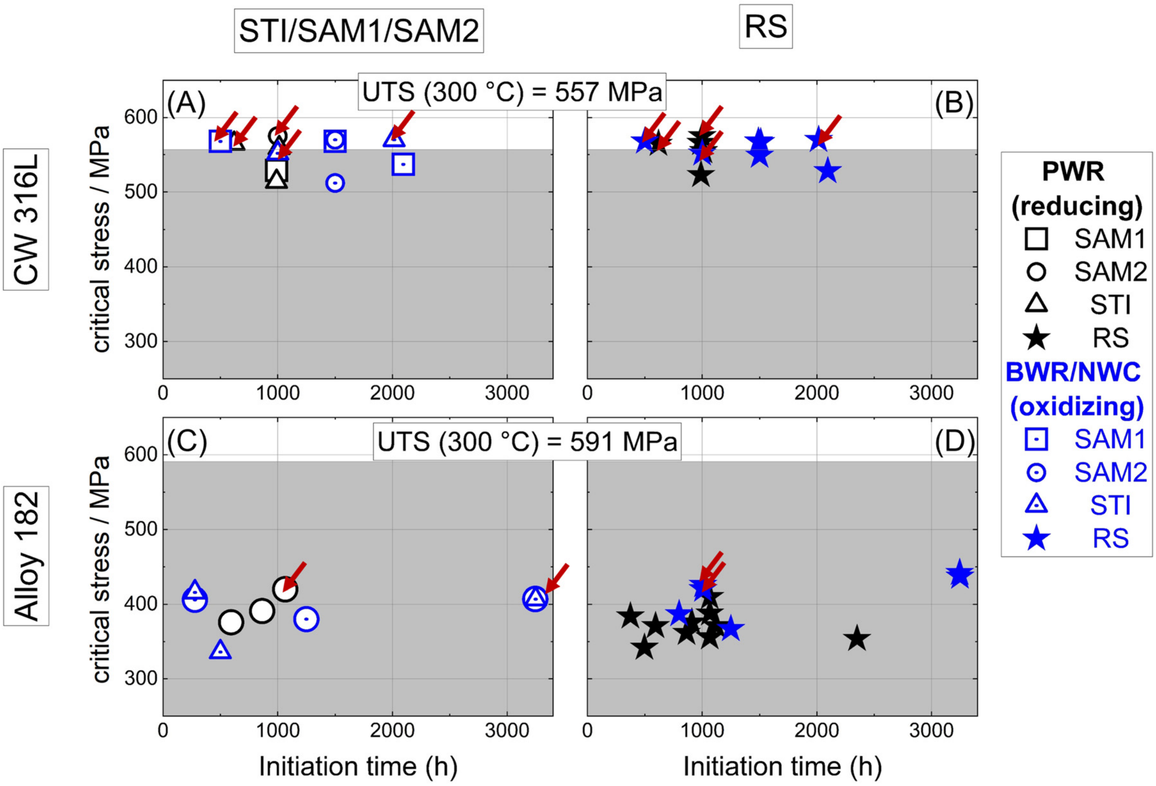

Figure 13: Critical stress versus initiation time plots for (A, B) CW 316L and (C, D) Alloy 182. Data points marked by red arrows represent the specimens which did not show SCC after corresponding time of CLT testing. Grey area in the graphs represents the UTS at 300 °C for both materials.

was suggested as an important contribution to the safe and economic long-term operation of LWRs worldwide.

5 Summary and conclusions

An extensive test campaign with structural materials under simulated LWR conditions was designed by the MEACTOS project consortium in order to study the mitigation of EAC by means of advanced surface treatments. More than a hundred CERT and CLT tests were performed covering about 4000 days of autoclave testing time (i.e. 10 years!). This paper summarises results of CERT and CLT EAC initiation tests conducted with austenitic CW 316L SS and Alloy 182 weld metal with four different surface treatments: RS = a ground surface selected as reference, STI = an industrial face-milled surface, SAM1 and SAM2 = advanced-machined surfaces without or with addition of lubricant. Flat tapered tensile specimens were subjected to CERT and CLT testing in both oxidizing (BWR/NWC) and reducing high-temperature water environments (PWR) at temperatures ranging from 288 to 360 °C. Tapered specimens allowed reliable EAC initiation testing under varying load conditions due to the gradual stress distribution and the possibility to calculate CC stress values from both CERT and CLT tests.

It should be noted that the results obtained by CERT tests are not relevant for in-service conditions. In-service materials' performance has more complex character which cannot be replicated by simple CERT testing.

The main results of this study can be summarised as follows:

- **Alloy 182:**
  - SCC initiation was observed during the CLT testing with applied stress levels corresponding to EAC threshold conditions determined from CERT testing in PWR and BWR/NWC environments. The CC stress determined from CLT testing was about 10 % lower than the one from CERT testing.
  - SCC initiation was accelerated using an increased temperature during CLT testing in PWR environment.
  - In oxidizing BWR/NWC environment, most cracks appeared on the STI surface, followed by the RS surface with the least number of cracks on the SAM2 surface.
  - In reducing PWR environment, most cracks were found on the RS and STI surfaces, with the least number on the SAM2 side.
  - In general, the EAC initiation susceptibility was slightly lower in BWR/NWC than in PWR primary water.
- **CW 316L:**
  - The 13 % CW 316L SS showed a significantly lower susceptibility to EAC initiation. At the start of the project, a level of CW of more than 10–15 % was regarded as irrelevant to plant conditions. The results of the project showed that the level of CW was either too low to sufficiently increase the EAC susceptibility of the 316L or the opposite effect could have taken place and this level was too high and therefore the corresponding EAC mechanism could not develop, which is very complex and needs a certain positive straining value as a necessary condition. Any surface treatment further contributes to local deformation and further deformation was not possible in this material.
  - SCC initiation was observed during the CLT testing with applied stress levels corresponding to EAC threshold conditions determined from CERT testing.
  - CC stress determined from CLT testing was about 10 % lower than that from CERT testing.
  - In oxidizing BWR environment, most cracks were found on the SAM1 surface, followed by the SAM2 and STI surfaces, with the least number on the RS surface.
  - In reducing PWR environment, equal crack occurrences were found on the RS, STI and SAM1 surfaces. No EAC occurred on the SAM2 surface.
  - No significant effect of surface treatment on the time-to-initiation could be revealed.
- The ANOVA analysis of the CERT results for Alloy 182 showed an effect of the nominal strain rate on the CC stress for EAC initiation. However, this effect was not pronounced in CW 316L, thus confirming the lower EAC susceptibility of CW 316L as compared to Alloy 182. The ANOVA analysis also did not show an effect of laboratory, confirming that CERT testing is a suitable methodology for accelerated EAC initiation testing. For CW 316L, the ANOVA analysis did not discern a surface finish effect whilst for Alloy 182 it did. This again confirms the lower EAC susceptibility for CW 316L compared to the nickel-based weld metal. The ANOVA analysis showed an effect of surface finish (RS versus STI for Alloy 182) which depended on the environment, i.e. the surface finish effect on CC stress, which differs in PWR and BWR/NWC.

Acknowledgments: The authors gratefully acknowledge the support from all involved members of the project consortium, especially to: Francisco "Paco" Perosanz Lopez, Ulla Ehrnstén, Renate Kilian, Alice Dinu, Claire

Rainasse, Jaromir Janousek, Mark Chatterton, Oliver Martin, Pedro Veron, Jonathan Duff, Michal Novak, Tim Austin, Thomas Pasutto, Alexandra Treichel, Aki Toivonen, Laura Molinero Merino, Krystian Wika and Prof. Grace Burke. The authors also acknowledge the support of the University of Bristol and particularly Dr. Tomas L. Martin during the manuscript preparation.

Author contributions: All the authors have accepted responsibility for the entire content of this submitted manuscript and approved submission.

Research funding: This project received funding from the Euratom research and training programme 2014–2018 under grant agreement no. 755151.

Conflict of interest statement: The authors declare that they have no competing interests regarding this article.

Data availability: The original test data and results of the CERT tests are available in the public domain (upon reasonable request) in the engineering database “MatDB” in the online data & information network of the EC Joint Research Centre (ODIN, https://odin.jrc.ec.europa.eu/odin/) (Ritter 2022b).

Abbreviations

ANOVA	analyses of variance
BF	bright field
BSE	back-scatter electron
BWR	boiling water reactor
CC stress	characteristic critical stress
CERT	constant extension rate tensile
CLT	constant load tensile
CW	cold-worked
EAC	environmentally-assisted cracking
EDM	electric discharge machining
EDS	energy dispersive X-ray spectrometry
LWR	light water reactor
MEACTOS	mitigating environmentally-assisted cracking through optimisation of surface condition
NWC	normal water chemistry
PWR	pressurised water reactor
RS	reference surface
SADP	selected area diffraction pattern
SAM1	advanced machining with supercritical CO2 cooling without lubrication
SAM2	advanced machining with supercritical CO2 cooling with dissolved minimum quantity lubrication oil
SCC	stress corrosion cracking
SE	secondary electron
SEM	scanning electron microscopy
SS	stainless steel
STI	standard industrial machining (face-milling)
TEM	transmission electron microscopy
UFGL	ultra-fine grained surface layer
UTS	ultimate tensile strength

References

Andresen, P.L. (2008). Emerging issues and fundamental processes in environmental cracking in hot water. Corrosion 64: 439–464.

Attanasio, S.A. and Morton, D.S. (2003). *Measurement of the nickel/nickel oxide transition in Ni-Cr-Fe alloys and updated data and correlations to quantify the effect of aqueous hydrogen on primary water scc*. Lockheed Martin Corporation, Schenectady, NY 12301 (US).

Bosch, R.-W., Ritter, S., Herbst, M., Kilian, R., Burke, M.G., Duff, J., Scenini, F., Gu, Y., Dinu, A., Ehrnstén, U., et al. (2021). Stress corrosion crack initiation testing with tapered specimens in high-temperature water – results of a collaborative research project. Corros. Eng. Sci. Technol. 56: 103–118.

Chang, L., Volpe, L., Wang, Y.L., Burke, M.G., Maurotto, A., Tice, D., Lozano-Perez, S., and Scenini, F. (2019). Effect of machining on stress corrosion crack initiation in warm-forged type 304L stainless steel in high temperature water. Acta Mater. 165: 203–214.

Couvant, T., Moulart, P., Legras, L., Bordes, P., Capelle, J., Rouillon, Y., and Balon, T. (2006). Pwscc of austenitic stainless steels of heaters of pressurizers. In: *Fontevraud 6 conference*, Avignon, France, pp. 67–78.

Du, D., Wang, J., Chen, K., Zhang, L., and Andresen, P.L. (2019). Environmentally assisted cracking of forged 316LN stainless steel and its weld in high temperature water. Corros. Sci. 147: 69–80.

Ford, F.P. and Andresen, P.L. (1994). *Corrosion in nuclear systems: environmentally assisted cracking in light water reactors*. In: Marcus P. and Ouder J. Marcel Dekker. pp. 501–546.

Gelman, A. (2005). Analysis of variance: why it is more important than ever. Ann. Math. Stat. 33: 1–53.

Gras, J. (1991). Stress corrosion cracking of steam generator tubing materials. In: *Review and assessment*. Electricite de France (EDF).

Griffiths, M. (2019). Ni-based alloys for reactor internals and steam generator applications. In: *Structural alloys for nuclear energy applications*. Elsevier, pp. 349–409.

Hojná, A., Halodová, P., Janoušek, J., and Zimina, M. (2020). Acceleration of environmentally assisted cracking initiation of the type 316L steel in high-temperature water and hydrogenated-steam vapor environments. Corrosion 76: 1177–1193.

Hojná, A., Zimina, M., Perosanz Lopez, F.J., Scenini F., Ritter, S., Vankeerberghen, M., Grimm, M., Dinu, A., Pasutto, T., Novotný, R., et al. (2022). Effect of surface treatment on environmentally-assisted crack initiation threshold of cold-worked type 316L in LWR environments. In: *Fontevraud 10: international symposium contribution of materials investigations and operating experience to LWRs’ safety, performance and reliability*, Avignon, France.

Horn, R., Gordon, G., Ford, F., and Cowan, R. (1997). Experience and assessment of stress corrosion cracking in L-grade stainless steel BWR internals. Nucl. Eng. Des. 174: 313–325.

Karlsen, W., Ivanchenko, M., Ehrnstén, U., Yagodzinskyy, Y., and Hänninen, H. (2009). Microstructural manifestation of dynamic strain aging in AISI 316 stainless steel. J. Nucl. Mater. 395: 156–161.

Kowaka, M. (1976). On the prevention of stress corrosion cracking in nuclear power plants. Zairyo 25: 1057–1067.

Lee, J., Jang, C., Kim, J.S., and Jin, T.E. (2007). Mechanical properties evaluation in inconel 82/182 dissimilar metal welds. In: *SMiRT 19*. Toronto, Canada.

Maziasz, P.J. and Busby, J.T. (2012). *Properties of austenitic stainless steels for nuclear reactor applications*. Oak Ridge National Lab.(ORNL), Oak Ridge, TN, USA.

Miki, M., Hamada, K., Ito, H., Kitamura, I., and Sasaki, R. (1978). Improvement of corrosion resistance of stainless steel pipes for BWR plant. Hitachi Hyoron 60: 93–98.

Moss, T., Kuang, W., and Was, G.S. (2018). Stress corrosion crack initiation in alloy 690 in high temperature water. Curr. Opin. Solid State Mater. Sci. 22: 16–25.

Mrp, E. (2004). *115, materials reliability program crack growth rates for evaluating primary water stress corrosion cracking (PWSCC) of Alloy 82, 182, and 132 welds (MRP-115)*. Report no. 1006696, chap. 4 and 6. Electric Power Rearch Institute, Palo Alto, CA.

Mulford, R. and Kocks, U. (1979). New observations on the mechanisms of dynamic strain aging and of jerky flow. Acta Metallurgica 27: 1125–1134.

Peng, K., Qian, K., and Chen, W. (2004). Effect of dynamic strain aging on high temperature properties of austenitic stainless steel. Mater. Sci. Eng.: A. 379: 372–377.

Que, Z., Volpe, L., Toivonen, A., Burke, M., Scenini, F., and Ehrnstén, U. (2021). Effects of surface treatments on environmentally-assisted cracking susceptibility of alloy 182 in BWR environment. Corros. Sci. 188: 109555.

Que, Z., Saario, T., Toivonen, A., and Ehrnstén, U. (2022a). Stress corrosion cracking initiation susceptibility of Alloy 182 with different surface treatments. Corros. Sci. 196: 110037.

Que, Z., Zajec, B., Ritter, S., Seppänen, T., Saario, T., Toivonen, A., Treichel, A., Lautaru, V., and Scenini, F. (2022b). Investigation of surface treatment effects on the environmentally-assisted cracking behaviour of Alloy 182 in boiling water reactor environment. Corros. Eng. Sci. Technol. 57: 474–485.

Ritter, S. (Ed.) (2020). *Nuclear corrosion: research, progress and challenges*. Woodhead Publishing on Behalf of the European Federation of Corrosion.

Ritter, S. (2022a). *Meactos - mitigating environmentally-assisted cracking through optimisation of surface condition*, Available at: <https://meactos.eu/> (Accessed 20 December 2022).

Ritter, S. (2022b). *MEACTOS environmentally-assisted crack initiation data for constant extension rate tensile tests in BWR/NWC and PWR environments on Alloy 182 Ni-based alloy and cold-worked 316L stainless steel*. European Commission, Available at: <https://odin.jrc.ec.europa.eu/odin/controller?query=DOICatalogViewer&p_DOI5=64>.

Robertson, J. (1989). The mechanism of high temperature aqueous corrosion of steel. Corros. Sci. 29: 1275–1291.

Scott, P.M. and Combrade, P. (2019). General corrosion and stress corrosion cracking of Alloy 600 in light water reactor primary coolants. J. Nucl. Mater. 524: 340–375.

Sleeswyk, A. (1958). Slow strain-hardening of ingot iron. Acta Metall. 6: 598–603.

Stahle, L. and Wold, S. (1989). Analysis of variance (ANOVA). Chemom. Intell. Lab. Syst. 6: 259–272.

Stellwag, B. (1998). The mechanism of oxide film formation on austenitic stainless steels in high temperature water. Corros. Sci. 40: 337–370.

Takaku, H. and Ushirogochi, T. (1977). Stress corrosion cracking behavior of stainless steels for nuclear reactor coolant pipings in high temperature water. Karyoku Genshiryoku Hatsuden (Japan) - KGH 28: 1079–1090.

Tribouilloy, L., Vaillant, F., Olive, J.-M., Puiggali, M., Legras, L., Couvant, T., Boursier, J., Rouillon, Y., and Amzallag, C. (2007). Stress corrosion cracking on cold-worked austenitic stainless steels in PWR environment. Adv. Mater. Sci. 7: 61–69.

Vaillant, F., Boursier, J.-M., Amzallag, C., Bibollet, C., and Pons, S. (2007). Environmental behaviour and weldability of Ni-base weld metals in PWRs. Revue Générale Nucléaire - RGN 6: 62–71.

Vankeerberghen, M. and Bosch, R.-W. (2022). Analysis of environmentally assisted crack initiation of Alloy 182 in simulated light water reactor primary water with the engineering initiation model enginit. Coross Eng. Sci. Technol. 57: 105–117.

Vankeerberghen, M., Bosch, R.-W., Dinu, A., Grimm, M., Hojna, A., Meadows, J., Novotny, R., Perosanz, F.-J., Que, Z., Ritter, S., et al. (2022). Some effects of surface finish and lwr environment on environmentally-assisted crack initiation in Alloy 182. In: *The 20th international conference on environmental degradation of materials in nuclear power systems-water reactor, 2022-07-17*. AMPP-NACE, Snowmass, Colorado, USA, pp. 1–23.

Volpe, L., Duff, J., Scenini, F. and Burke, G. (2020). Exploring the effect of surface machining treatments on microstructure of cold-rolled type 316L austenitic stainless steel and Alloy 182. In: *EUROCORR 2020*, (virtual congress).

Volpe, L., Curioni, M., Burke, M.G., and Scenini, F. (2021). Thermodynamic equivalence charts for stress corrosion cracking studies in hydrogenated steam, high pressure and supercritical water. J. Electrochem. Soc. 168: 011501.

Volpe, L., Burke, G., Zaiqing, Q., Ehrnstén, U., Treichel, A., Ritter, S., Hojna, A., Herbst, M., Kilian, R., Maurotto, A., et al. (2022). Exploring the influence of surface machining treatments on microstructure and environmentally assisted cracking on Alloy 182. In: *The 20th international conference on environmental degradation of materials in nuclear power systems-water reactor*. Snowmass, CO, USA.

Yonezawa, T. (2012). Nickel alloys: properties and characteristics. In: *Comprehensive nuclear materials*. Elsevier, pp. 233–266.